

RESEARCH LETTER

10.1002/2015GL064373

Key Points:

- The importance of both large-scale dynamics and local feedback for sea-ice melt
- The location of extra melt near the ice edge, due to the air-mass transformation
- The role of clouds, longwave radiation and turbulent heat flux for sea-ice melt

Supporting Information:

- Figure S1
- Figure S2
- Figure S3
- Figure S4
- Text S1

Correspondence to:

M. Tjernström,
michaelt@misu.su.se

Citation:

Tjernström, M., et al. (2015), Warm-air advection, air mass transformation and fog causes rapid ice melt, *Geophys. Res. Lett.*, 42, 5594–5602, doi:10.1002/2015GL064373.

Received 29 APR 2015

Accepted 9 JUN 2015

Accepted article online 10 JUN 2015

Published online 4 JUL 2015

©2015. The Authors.

This is an open access article under the terms of the Creative Commons Attribution License, which permits use, distribution and reproduction in any medium, provided the original work is properly cited.

Warm-air advection, air mass transformation and fog causes rapid ice melt

Michael Tjernström¹, Matthew D. Shupe^{2,3}, Ian M. Brooks⁴, P. Ola G. Persson^{2,3}, John Prytherch⁴, Dominic J. Salisbury⁴, Joseph Sedlar¹, Peggy Achtert⁴, Barbara J. Brooks⁵, Paul E. Johnston^{2,3}, Georgia Sotiropoulou¹, and Dan Wolfe^{2,3}
¹Department of Meteorology and Bolin Centre for Climate Research, Stockholm University, Stockholm, Sweden,

²Cooperative Institute for the Research in Environmental Sciences, University of Colorado Boulder, Boulder, Colorado, USA,

³Earth System Research Laboratory, National Oceanic and Atmospheric Administration, Boulder, Colorado, USA, ⁴School of Earth and Environment, University of Leeds, Leeds, UK, ⁵National Centre for Atmospheric Science, University of Leeds, Leeds, UK

Abstract Direct observations during intense warm-air advection over the East Siberian Sea reveal a period of rapid sea-ice melt. A semistationary, high-pressure system north of the Bering Strait forced northward advection of warm, moist air from the continent. Air-mass transformation over melting sea ice formed a strong, surface-based temperature inversion in which dense fog formed. This induced a positive net longwave radiation at the surface while reducing net solar radiation only marginally; the inversion also resulted in downward turbulent heat flux. The sum of these processes enhanced the surface energy flux by an average of $\sim 15 \text{ W m}^{-2}$ for a week. Satellite images before and after the episode show sea-ice concentrations decreasing from $> 90\%$ to $\sim 50\%$ over a large area affected by the air-mass transformation. We argue that this rapid melt was triggered by the increased heat flux from the atmosphere due to the warm-air advection.

1. Introduction

The most pronounced and robust observation of Arctic climate-change is the reduction in area and thickness of perennial sea ice [Holland and Bitz, 2003; Serreze and Barry, 2011]. Arctic sea-ice cover displays a declining trend over the entire satellite record [Serreze et al., 2007]. While this trend occurred for all seasons, with an average area reduction of $\sim 4\%$ per decade, the most pronounced reduction has been in summer, about 12% per decade [e.g., Intergovernmental Panel on Climate Change (IPCC), 2013]. Additional to the long-term trend, there is considerable interannual variability [Serreze et al., 2007; Cavalieri and Parkinson, 2012; Kapsch et al., 2013]; the extreme low-ice summers of 2007 and 2012 attracted great attention [Kay et al., 2008; Graversen et al., 2011; Simmonds and Rudeva, 2012; Devasthale et al., 2013; Parkinson and Comiso, 2013]. The decreasing sea ice has important consequences for the climate system and for society [e.g., Arctic Climate Impact Assessment, 2004; International Study on Arctic Change, 2010; Snow, Water, Ice and Permafrost in the Arctic, 2011]. Shrinking ice leads to an increasing importance of marginal ice zone (MIZ); hence, there is a growing interest in physical processes governing the MIZ [e.g., Zhang et al., 2012]. Prediction of sea ice is also a growing area of research [Day et al., 2014; Kapsch et al., 2014; also see the “Sea Ice Outlook,” <http://www.arcus.org/sipn/sea-ice-outlook>], as is the potential for navigation of northern sea routes and exploitation of marine natural resources.

While there is broad consensus that sea-ice decline is a manifestation of anthropogenic climate change [Min et al., 2008; IPCC, 2013], contributing to an “Arctic amplification” of that change [Serreze and Francis, 2006; Serreze and Barry, 2011], there is limited consensus on the processes responsible. Proposed hypotheses can be divided into external forcing and internal feedbacks. Examples of the former are changes in meridional atmospheric transport of heat and/or moisture [Graversen et al., 2008, 2011; Kapsch et al., 2013; Cai and Tung, 2012] or oceanic inflow of heat [Shimada, 2006; Polyakov et al., 2007]. Examples of internal feedback processes are clouds and aerosols [Kay and Gettelman, 2009; Mauritsen et al., 2011; Liu and Key, 2014], boundary layer processes [Bintanja et al., 2011], and factors affecting surface albedo such as sea-ice melt [Perovich et al., 2007], melt ponds [Schröder et al., 2014], or snow melt [Fletcher et al., 2009a, 2009b].

Most studies of this changing system are based on satellite data, atmospheric reanalyses, and/or modeling; however, all of these have drawbacks. Satellite products rely on uncertain retrieval algorithms and lack

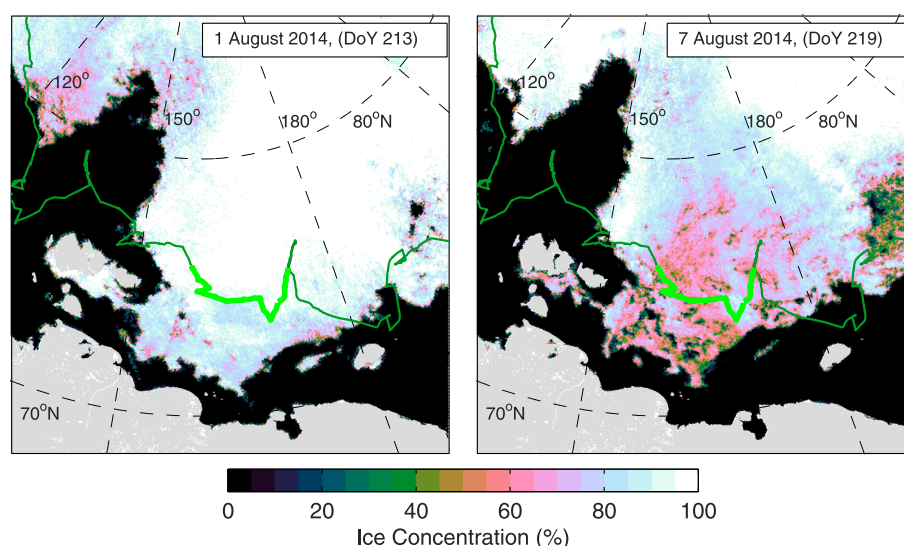


Figure 1. Sea ice maps showing ice concentration for 1 and 7 August 2014. ARTIST Sea Ice (ASI) algorithm (from AMSR2) version 5.2, grid 6.25 km, from University of Bremen. Green line shows the track of *Oden* with days of particular interest highlighted.

vertical resolution. Reanalyses suffer from lack of observations and uncertain model physics and do not include ocean/ice/atmosphere coupling. Climate models further suffer from uncertain model physics and display very large intermodel differences in the Arctic [Bony *et al.*, 2006; Meehl *et al.*, 2006]. Only few observational data sets exist that can be used to understand key processes: Surface Heat Budget of the Arctic Ocean (SHEBA) [Uttal *et al.*, 2002], Arctic Ocean Experiment 2001 (AOE-2001) [Tjernström, 2005], Arctic Summer Cloud Ocean Study (ASCOS) [Tjernström *et al.*, 2014]. Of these only SHEBA covers an annual cycle and none cover more than 1 year.

One transient atmospheric process considered in several recent studies is advection of warm and moist air from south [Sedlar and Devasthale, 2012; Devasthale *et al.*, 2013; Kapsch *et al.*, 2013; Pithan *et al.*, 2014; Woods *et al.*, 2013]. However, very few cases have been documented by direct observations [Perovich *et al.*, 2003; Tjernström, 2005; Persson, 2012]. Most studies are either from winter, when solar radiation is negligible, or focus on the seasonal transitions between melt and freeze; none are from the MIZ.

In this paper we report on a warm-air advection episode in early August 2014, observed during the *Arctic Clouds in Summer Experiment* (ACSE) in the East Siberian Sea, at a time of rapid ice melt. Figure 1 shows sea-ice concentration from Advanced Microwave Scanning Radiometer 2 (AMSR2) [Spreen *et al.*, 2008] on day of year (DOY) (defined 1.0 at 00 UTC on 1 January; all times given in UTC) 213 and 219 (1 and 7 August), for the region of interest. Over this time, the southern edge of a broad ice tongue between the New Siberian Islands and Wrangel Island, reaching almost down to the continent, moved only slightly northward, while sea-ice concentration experienced a rapid decrease over a large region. Shipboard observations allowed us to document how this warm-air advection and feedbacks from the consequent air-mass transformation created conditions conducive for triggering rapid sea-ice melt as warm air moved over melting sea ice.

2. Observations and Methods

ACSE was part of the *Swedish-Russian-US Arctic Ocean Investigation on Climate-Cryosphere-Carbon* (SWERUS-C³) expedition on the Swedish icebreaker *Oden*. SWERUS-C³ started in Tromsø, Norway, on 5 July 2014 and transected the Kara, Laptev, East Siberian, and Chukchi Seas, mostly on the Siberian shelf, arriving in Barrow on 19 August. A second leg started on 20 August and continued back to Tromsø, somewhat farther north, ending on 5 October; Figure 2 shows the expedition track.

While the overarching motivation for SWERUS-C³ was to study Arctic Ocean carbon cycles, a primary objective of ACSE was to study Arctic clouds, their interaction with the tropospheric vertical structure,

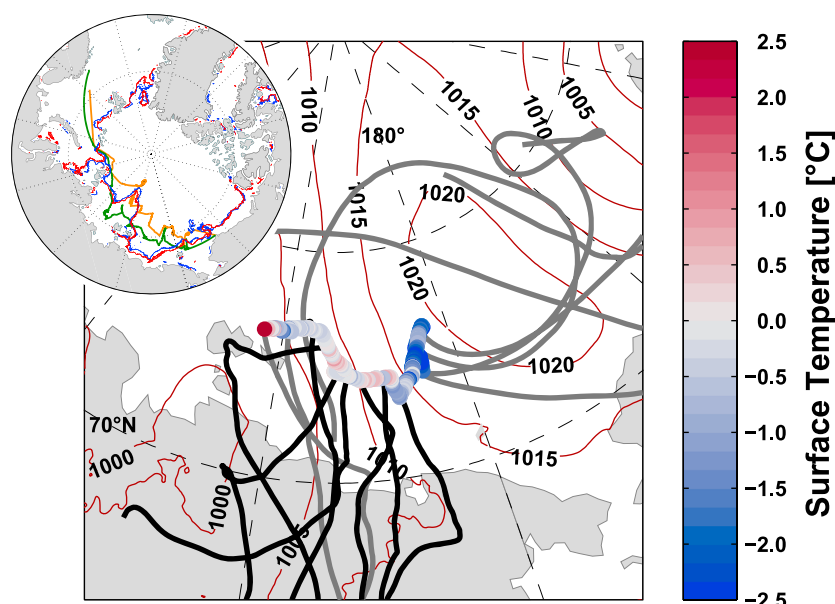


Figure 2. Maps of the area of interest showing (thick colored dots) cruise track, (thin brown) isobars for DOY 214 (4 August) 2014 and (thick black and gray; attached to track) 5 day back trajectories with receptor points at *Oden's* location at 600 m on 00 UTC each day. Upper left insert shows the expedition cruise track for (green) the first and (yellow) the second legs, and the edge of the sea ice (blue) before and (red) after the episode. Black trajectories are calculated for the main episode, while gray trajectories are from before and after the episode.

response to meridional transport of air from south, and effect on the surface energy balance, and hence the ice, during the summer melt and early autumn freezeup. These goals were accomplished by deploying instruments on *Oden*; the instrument suite was largely modeled after ASCOS in 2008 [Tjernström *et al.*, 2014], also on *Oden*, differing only in that all instruments were installed on board during ACSE.

The remote sensing instrument suite included a W-band Doppler cloud radar, a 449 MHz wind-profiling radar, a scanning Doppler lidar, and scanning multiwavelength microwave radiometers. In situ observations comprised eddy-covariance turbulent flux measurements on a mast at the bow of the ship, a weather station on the top-deck of the ship, and 6-hourly radiosondes. Additional instruments include incoming shortwave and longwave radiation, laser cloud ceilometers, and visibility sensors. Ship-borne deployment prohibits observations of upwelling surface radiation; we estimate surface emitted longwave radiation from the surface skin temperature observed with two infrared temperature sensors viewing the surface in two directions from the top deck. Surface albedo is estimated from assessing fractional coverage of open water, sea ice, snow, and melt ponds using web camera images using estimates of the albedo of each surface type [e.g., Perovich *et al.*, 2002; Persson *et al.*, 2002].

3. Results

3.1. Large-Scale Atmospheric Setting

Oden entered pack ice near Bennett Island late DOY 210 (29 July) and remained in the ice until late DOY 222 (10 August). Sea-ice concentrations (Figure 1) were initially high (>95%), with thick multiyear ice, especially in the southern portion of the track. Figure 2 shows the general weather situation. A semistationary high-pressure system to the east and a low-pressure trough to the west, in which a series of low-pressure systems passed north during the start of the episode, facilitated an uninterrupted southerly flow over the area. Daily 5 day back trajectories, with receptor points 600 m above *Oden's* location at 00 UTC, show air-mass origins from the eastern Siberian continent. The temperature over the northeast Siberian coast was up to 6°C warmer than the 1981–2010 average (National Center for Atmospheric Research/National Centers for Environmental Prediction reanalysis, <http://www.esrl.noaa.gov/psd/>).

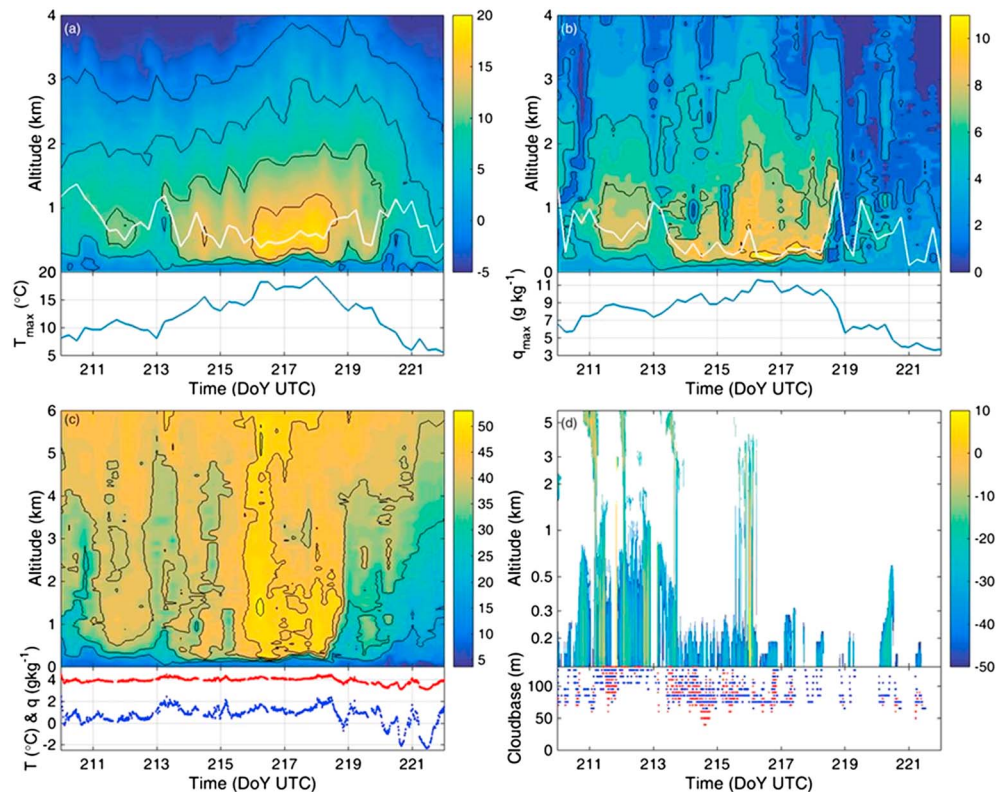


Figure 3. Time-height cross-sections of (a) temperature ($^{\circ}\text{C}$), (b) specific humidity (g kg^{-1}), (c) equivalent potential temperature ($^{\circ}\text{C}$), and (d) cloud radar reflectivity (dBZ). Below each cross section is additional information: In Figures 3a and 3b the maximum temperature ($^{\circ}\text{C}$) and specific humidity (g kg^{-1}) in the vertical (altitudes are indicated with white lines in each cross section), in (Figure 3c) near surface temperature and specific humidity ($^{\circ}\text{C}$ and g kg^{-1}), and in (Figure 3d) the lowest cloud base (m). Note the logarithmic altitude scale in (Figure 3d).

The period of interest starts on DOY 211 (30 July) with the passing of a frontal system (Figures 3c and 3d and Figures S1a and S2a in the supporting information); this first low-pressure system was followed by weak warm fronts over the next days. After a frontal passage on DOY 213 (Figures 3 and S1b) the air flow was southerly, supported by the pressure gradient between a blocking high to the east and a trough to the west (see Figures 2 and S2c). Another significant frontal system passed near *Oden* during the night DOY 215–216 (Figures 3c and 3d). The episode ended with a cold front late DOY 219 (Figures 3, S1d, and S2d), changing the airflow to come from northeast. Hence, during DOY 213 through 217 the air came more or less directly from eastern Siberia; DOY 211–212 (before) and DOY 218–219 (after) were transition periods.

3.2. Air Mass Adjustment

Time-height cross-sections of atmospheric temperature, moisture, equivalent potential temperature, and cloud radar reflectivity are shown in Figure 3. Figure 3a indicates a 2 day warm pulse (DOY 211–212) associated with the first low-pressure system, with elevated but roughly constant maximum temperature around 10°C at $\sim 500\text{ m}$. This was followed by increasing temperatures in the lower troposphere from early DOY 213, peaking at $\sim 19^{\circ}\text{C}$ around 500 m on DOY 218.0. Except for during the first warm-air pulse maximum specific moisture (Figure 3b) occurred below the temperature maximum; humidity also peaked earlier, at 11.7 g kg^{-1} , on DOY 216.5, before declining first slowly and from DOY 218 more rapidly.

As the warm continental air advected over the melting sea ice, with a near-surface air temperature only slightly above 0°C (Figure 3c), a strong temperature inversion formed. During the core event (DOY 213 through 217), the surface inversion was $\sim 10\text{--}20^{\circ}\text{C}$ over about 500 m , although turbulent mixing reduced the vertical temperature gradient in the lowest $\sim 100\text{ m}$. Specific humidity more than doubled, from $\sim 4\text{ g kg}^{-1}$ near the surface to $\sim 9\text{ g kg}^{-1}$ at about 300 m , while the wind speed profile featured a low-level

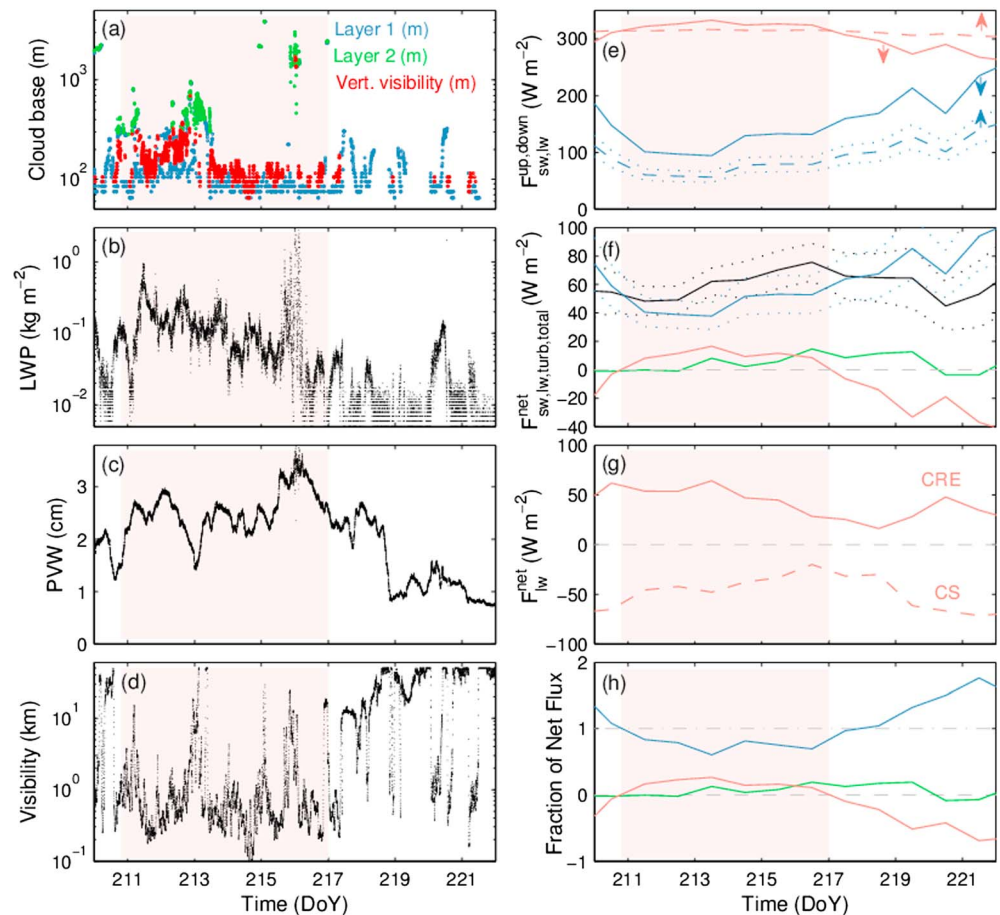


Figure 4. Time series of (a–d) variables related to the clouds and (e–h) daily averaged surface energy fluxes: Figure 4a shows cloud base heights and vertical visibility (m); Figure 4b shows LWP (kg m⁻²); Figure 4c shows PWV (cm); Figure 4d shows horizontal visibility (km); Figure 4e downwelling (solid) and upwelling (dashed) longwave (red) and solar (blue) radiation; Figure 4f shows net longwave (red) and solar (blue) radiation, and sum of turbulent sensible and latent heat fluxes (green), and total energy flux (black); Figure 4g shows net clear sky longwave (dashed) and surface cloud radiation effect (solid); and Figure 4h shows the net solar (blue), longwave (red), and turbulent (green) heat fluxes as fractions of the total surface energy flux. All energy fluxes are in W m⁻², and except in (e), positive fluxes are downward. Upwelling and net solar radiation and total energy flux assume an albedo of 60%; dotted lines indicate ±10% about this. In Figure 4a, multiple values of cloud base height are given when lowest layers cover less than 100% of the sky: lowest cloud base in blue and second lowest in green, while vertical visibility (red) is only indicated for dense fog. The shaded region indicates the period with positive surface net longwave radiation.

jet with a maximum of 8–17 m s⁻¹ at 200–400 m (Figure S3). The jet was likely an inertial oscillation initiated at the ice edge as the turbulent surface momentum flux changed abruptly when warm continental air entered over the cooler melting pack ice. The wind direction through the lowest kilometers of the troposphere was in the southerly sector (140–200°, not shown). This vertical structure bears the clear footprint of an air-mass transformation, from a deep well-mixed continental boundary layer upstream to a quasi-equilibrium farther downstream, with the shallow well-mixed cloud- and inversion-capped boundary layer with near-zero turbulent heat fluxes at the surface, commonly observed in the central Arctic in summer [e.g., Tjernström *et al.*, 2012].

3.3. Clouds

The height of maximum humidity (Figure 3b) roughly coincided with the top of a layer of fog or low clouds (Figure 3d). Cloud base heights, liquid water path (LWP), precipitable water vapor (PWV), and horizontal visibility are shown in Figures 4a–4d. PWV is the column-integrated water vapor. Water vapor is an important greenhouse gas; it also facilitates cloud formation. LWP (column integrated cloud liquid water)

larger than 0.05 kg m^{-2} indicates clouds acting as a black body. Low clouds appeared late on DOY 210 (29 July); over the next days the visibility indicated several foggy periods, while LWP increased slightly. On DOY 211, LWP, and PWV increased abruptly, by an order of magnitude and a factor of 2, respectively, while visibility and cloud base height remained very low until DOY 213.0.

During DOY 213.5–217.5, low clouds/fog dominated, with tops around 200–300 m (Figures 3d and 4a), about half to two thirds of the surface-inversion depth. Visibility remained $< 1 \text{ km}$, and briefly dropped to $< 100 \text{ m}$ on DOY 214. Around DOY 216.0 deeper clouds, associated with a frontal passage, occurred; after this the low cloud layer became more intermittent, and LWP was reduced. However, the warm-air advection continued until DOY 218.0 (Figure 3a); PWV then dropped and the episode was effectively over. In summary the warm air advection episode started with deeper clouds (DOY 210–213) was then dominated by boundary-layer clouds and fog (DOY 213–216) and finally by low clouds with periods of clear skies (DOY 216–219).

3.4. Surface Energy Balance

Our estimate of the surface energy balance (SEB) (Figures 4e–4h) includes radiation fluxes and turbulent latent and sensible heat fluxes; fluxes are defined positive downward. Data were quality controlled, removing data affected by disturbance or shading from *Oden*. Useful data was obtained for about 80% of the time, except for latent heat flux that was recovered roughly 40% of the time due to known difficulties in observing moisture in the Arctic [Persson *et al.*, 2002; Tjernström *et al.*, 2014]. Daily averages were computed for each term before combining into net fluxes (Figures 4e–4f). The most uncertain term is upwelling shortwave radiation (Figure 4e), calculated from downwelling radiation and estimated albedo, α . We show results using $\alpha = 60\% \pm 10\%$ —reasonable estimates of the mean, lower, and upper bounds from reviewing webcam images [e.g., Perovich *et al.*, 2002]. Albedo variations depended mostly on melt ponds and snow on the ice; open water was rare at this time.

Downwelling longwave radiation was larger than upwelling DOY 210.8–217 (Figure 4e), a consequence of the low and warm clouds. An atmosphere warmer than the surface provides a necessary but not sufficient condition for downward net longwave radiation; clouds provide a substantially higher emissivity compared to clear air, necessary for positive net longwave radiation (Figure 4f). Using the Rapid Radiative Transfer Model (RRTM) code [Mlawer *et al.*, 1997], using atmospheric profiles from radiosoundings as input, provides estimates of clear-sky net longwave radiation and net longwave surface cloud radiative effect (CRE_{LW}) (Figure 4g). The clear-sky net longwave radiation was negative before the episode, around -70 W m^{-2} , increasing to about -20 W m^{-2} by DOY 216.5. Then, as a consequence of the drier air arriving aloft, it decreased after DOY 217, although the temperature continued to increase for one more day; the decrease became more rapid as temperature decreased after DOY 219. CRE_{LW} was initially $\sim 55 \text{ W m}^{-2}$ but decreased after DOY 213.5 to $\sim 25 \text{ W m}^{-2}$. The combination of CRE_{LW} initially and increasing clear-sky radiation later combined to keep net longwave radiation positive DOY 211.0 to DOY 217.0.

Net shortwave radiation decreased during the period, compared to before and after. This reduction was $\sim 20 \text{ W m}^{-2}$ initially, decreasing slightly with time (Figure 4f). Although the sun remained above the horizon throughout the episode, there was a distinct diurnal cycle in net surface radiation (Figure S4), with large positive values at local noon and lower values with the sun low in the sky. During this episode daily maximum net radiation decreased slightly but remained positive throughout the diurnal cycle; daily periods of negative net radiation were observed before and after. The turbulent heat flux (Figure 4f) was small initially but increased as the surface inversion strengthened and wind speed increased and became about as large as the net longwave radiation during DOY 216 and remained high until DOY 219. These factors together contributed to an increase in surface heat flux. SEB changes over time are similar for the limiting albedo assumptions, although absolute values differ within about $\pm 10 \text{ W m}^{-2}$. Comparing to conditions before and after, this event included an additional surface energy surplus of $30\text{--}40 \text{ W m}^{-2}$ at maximum (Figure 4f).

We also calculated the relative contribution of the net shortwave and longwave radiation and turbulent energy fluxes to the total flux (Figure 4h). During the core episode the net shortwave contribution dropped to 60–80%, while the contribution from net longwave radiation and turbulent heat fluxes increased from negative and zero contributions, respectively, to 10–20%. The contribution from the sum of these two fluxes peaked at about 40% during DOY 213. Hence, while it is clear that solar radiation is the

largest contributor to the net surface energy flux, as expected at this time of the year, the other two fluxes significantly contribute to the surface energy flux during the core episode.

The CRE_{LW} could arguably have been larger if the clouds had been higher into the inversion where temperatures were higher; the clouds shielded the surface from the highest temperatures. However, the fog formed as air near the surface was cooled from below passing over the melting sea ice and was confined to low levels by the resulting high static stability caused by advection of warm air aloft, maintaining the inversion structure. LWP values indicate that there must have been substantial cloud-top cooling, at least up to DOY 216. This cooling was likely balanced by a combination of latent heat of condensation and horizontal advection, maintaining the cloud and inversion. Turbulent mixing could also have contributed. Although static stability was large, the wind shear was substantial (e.g., Figure S3). Hence, as indicated by observations from the Doppler radar (not shown), cloud-top cooling did not lead to substantial turbulence production. For fog to lift to low stratus clouds, common for central Arctic [e.g., *Tjernström et al.*, 2012], would require stronger vertical mixing than observed [e.g., *Shupe et al.*, 2013]. These more elevated clouds typically include a shallow well-mixed cloud-capped boundary layer with an inversion at cloud top and hence slightly lower temperature at cloud base than at surface.

4. Conclusions and Discussion

Previous studies highlighted the importance of episodic meridional transport of warm and moist air over the Arctic, for the onset of seasonal melt [*Persson*, 2012; *Woods et al.*, 2013] and for the near-zero peak in the winter bimodal net-radiation probability distribution [*Morrison et al.*, 2012]. *Graversen et al.* [2011] and *Sedlar and Devasthale* [2012] attributed the 2007 record ice melt to large-scale warm-air advection; *Kapsch et al.* [2013] argued the importance of longwave forcing by warm and moist air, and clouds, in springtime, preconditioning the ice in years with large melt. The majority of these studies were derived from modeling, reanalysis, and/or satellite information. Previous in situ observations of summer warm-air advection summer events over the Arctic pack ice are from well within the pack ice, e.g., SHEBA [*Persson*, 2012], AOE-2001 [*Tjernström et al.*, 2004] and ASCOS [*Sedlar et al.*, 2011]. To our knowledge a detailed observational account of an air-mass transformation event like the one presented here has not been published before.

Using direct observations, we show a combination of factors that came together in the East Siberian Sea in summer 2014 to trigger enhanced ice melt. An important conclusion is that external forcing and local feedbacks were both important. Warm atmospheric temperatures and a strong surface inversion were a consequence of persistent advection of continental air and air-mass transformation over the melting sea ice. Formation of low-level cloud and fog was a direct consequence of near-surface cooling of air during this transformation; enhanced surface radiative effects came from the combination of the temperature inversion and fog/clouds. The inversion combined with persistent southerly flow due to the low-level jet drove the downward turbulent heat flux. The resulting vertical structure is indicative of this air-mass transformation, and it was the combination of all of these factors that provided the additional energy input at the ice surface.

We were only able to observe these processes at one, although approximately constant, distance downstream of the coast (Figures 1 and 2). The fact that we see a diurnal variation in the temperature near the inversion top and also in the wind-speed at maximum, as well as the presence of a nearly moist-neutral layer aloft (Figure S3c), lends credibility to our conclusion that the factors discussed above were an inevitable result of an air-mass transformation that could only occur at the periphery of the ice pack. Already at the distance from the coast where *Oden* was navigating, reduced static stability by turbulent mixing is evident in the near-surface layer, clearly seen in the soundings (Figure S3a–c). Further into the central Arctic, continued air-mass adjustment would eventually lead to a well-mixed, cloud-capped, boundary layer with the inversion base near cloud top [*Tjernström et al.*, 2012]. The turbulent flux of sensible heat would tend to near zero [*Tjernström et al.*, 2012], while the cloud base would have a slightly lower temperature than the surface. Although the clouds could still warm the surface compared to clear skies, depending on the surface albedo, the net longwave radiation at the surface would be smaller than was observed here.

Our analysis of the SEB, indicating an additional surface warming of $\sim 30\text{--}40\text{ W m}^{-2}$ at its peak, is likely an underestimate since it is based on a fixed surface albedo. In reality, the surface melt should have reduced the albedo over time, giving an increasing warming over time. The actual impact on the sea ice is however difficult to ascertain. An extra 20 W m^{-2} surface heating would theoretically melt an additional $\sim 4\text{--}5\text{ cm}$ of ice over 7 days, assuming horizontally homogeneous slab ice; in reality melting is unevenly distributed, larger where surface albedo is lower. The ice concentration in a large area, corresponding to that exposed to the warm air advection, decreased from $\sim 90\text{--}95\%$ to around $50\text{--}60\%$ (Figure 1). This was consistent with anecdotal information from *Oden's* crew, reporting a transition from large cohesive ice floes with intact melt ponds, causing difficulties for navigation, to patchier ice floes with melt ponds melted through providing for easier ice breaking. It is not possible to quantify the contribution of the enhanced heat flux to the decrease in ice concentration; there would have been seasonal melt regardless. Ice dynamics may also have contributed; however, the main change occurred in sea-ice concentration and not in sea-ice extent. The fact that the southern ice edge moved only marginally northward and that features in the ice cover, such as local areas with lower concentration south of *Oden's* track, remained roughly stationary through the event indicates that ice dynamics may not have contributed greatly.

It should be noted that this is one single event and does not represent climate. Still, the sequence of events recorded on location serves to illustrate the complexity of important, interlinked processes on different scales. To understand the broader implications of such events, our analysis could be repeated using reanalysis products. However, that raises the question of how well atmospheric models capture the processes discussed here. In particular, the formation of strong surface inversions and low clouds present significant modeling challenges, especially for climate models with poor vertical resolution. Further, comprehensive observations on several scales are needed to improve the representation of sea-ice energy budget and melting processes in models.

Acknowledgments

We acknowledge funding from the Knut and Alice Wallenberg Foundation, Swedish Research Council, US Office of Naval Research, US National Oceanic and Atmospheric Administration (NOAA), and the UK Natural Environment Research Council. Instruments were supplied by the Earth System Research Laboratory of NOAA in Boulder, Colorado and the UK National Centre for Atmospheric Science. We are grateful to the Swedish Polar Research Secretariat and the two crews of the *Oden* and their Captains for logistics support. All data from ACSE will be made available through the Bolin Centre for Climate Research database (<http://www.bolin.su.se>).

The Editor thanks two anonymous reviewers for their assistance in evaluating this paper.

References

- Arctic Climate Impact Assessment (2004), *Impacts of a Warming Arctic: Arctic Climate Impact Assessment*, 1020 pp., Cambridge Univ. Press, Cambridge.
- Bintanja, R., R. G. Graversen, and W. Hazeleger (2011), Arctic winter warming amplified by the thermal inversion and consequent low infrared cooling to space, *Nat. Geosci.*, *4*, 758–761, doi:10.1038/NGEO1285.
- Bony, S., et al. (2006), How well do we understand and evaluate climate change feedback processes?, *J. Clim.*, *19*, 3445–3482, doi:10.1175/JCLI3819.1.
- Cai, M., and K.-K. Tung (2012), Robustness of dynamical feedbacks from radiative forcing: 2% solar versus $2 \times 3\text{ CO}_2$ experiments in an idealized GCM, *J. Atmos. Sci.*, *69*, 2256–2271, doi:10.1175/JAS-D-11-0117.1.
- Cavalieri, D. J., and C. L. Parkinson (2012), Arctic sea ice variability and trends, 1979–2010, *Cryosphere*, *6*, 881–889, doi:10.5194/tc-6-881-2012.
- Day, J. J., S. Tietsche, and E. Hawkins (2014), Pan-Arctic and regional sea ice prediction: Initialisation month dependence, *J. Clim.*, *27*, 4371–4390, doi:10.1175/JCLI-D-13-00614.1.
- Devasthale, A., J. Sedlar, T. Koenig, and E. J. Fetzer (2013), The thermodynamic state of the Arctic atmosphere observed by AIRS: Comparisons during the record minimum sea ice extents of 2007 and 2012, *Atmos. Chem. Phys.*, *13*, 7441–7450, doi:10.5194/acp-13-7441-2013.
- Fletcher, C. G., S. C. Hardiman, P. J. Kushner, and J. Cohen (2009a), The dynamical response to snow cover perturbations in a large ensemble of atmospheric GCM integrations, *J. Clim.*, *22*, 1208–1222, doi:10.1175/2008JCLI2505.1.
- Fletcher, C., P. Kushner, A. Hall, and X. Qu (2009b), Circulation responses to snow albedo feedback in climate change, *Geophys. Res. Lett.*, *36*, L09702, doi:10.1029/2009GL038011.
- Graversen, R. G., T. Mauritsen, M. Tjernström, E. Källén, and G. Svensson (2008), Vertical structure of recent Arctic warming, *Nature*, *451*, 53–57.
- Graversen, R. G., T. Mauritsen, S. Drijfhout, M. Tjernström, and S. Mårtensson (2011), Warm winds from the Pacific caused extensive Arctic sea-ice melt in summer 2007, *Clim. Dyn.*, *36*, 2103–2112, doi:10.1007/s00382-010-0809-z.
- Holland, M. M., and C. M. Bitz (2003), Polar amplification of climate change in coupled models, *Clim. Dyn.*, *21*, 221–232, doi:10.1007/s00382-003-0332-6.
- Intergovernmental Panel on Climate Change (IPCC) (2013), Summary for policymakers, in *Climate Change 2013: The Physical Science Basis. Contribution of Working Group I to the Fifth Assessment Report of the Intergovernmental Panel on Climate Change*, edited by T. F. Stocker et al., Cambridge Univ. Press, Cambridge, U. K., and New York.
- International Study on Arctic Change (2010), *International Study on Arctic Change: Science Plan and Implementation Strategy*, edited by M. S. Murray et al., ISAC International Program Office, Stockholm. [Available at <http://www.arcticchange.org/publications>.]
- Kapsch, M.-L., R. G. Graversen, and M. Tjernström (2013), Springtime atmospheric energy transport and the control of Arctic summer sea-ice extent, *Nat. Clim. Change*, *3*, 744–748, doi:10.1038/nclimate1884.
- Kapsch, M.-L., R. G. Graversen, T. Economou, and M. Tjernström (2014), The importance of spring atmospheric conditions for the prediction of Arctic summer sea-ice extent, *Geophys. Res. Lett.*, *41*, 5288–5296, doi:10.1002/2014GL060826.
- Kay, J. E., and A. Gettelman (2009), Cloud influence on and response to seasonal Arctic sea ice loss, *J. Geophys. Res.*, *114*, D18204, doi:10.1029/2009JD011773.
- Kay, J. E., T. L. 'Ecuyer, A. Gettelman, G. Stephens, and C. O'Dell (2008), The contribution of cloud and radiation anomalies to the 2007 Arctic sea ice extent minimum, *Geophys. Res. Lett.*, *35*, L08503, doi:10.1029/2008GL033451.
- Liu, Y., and J. R. Key (2014), Less winter cloud aids summer 2013 Arctic sea ice return from 2012 minimum, *Environ. Res. Lett.*, *9*, 044002, doi:10.1088/1748-9326/9/4/044002.
- Mauritsen, T., et al. (2011), An Arctic CCN-limited cloud-aerosol regime, *Atmos. Chem. Phys.*, *11*, 165–173, doi:10.5194/acp-11-165-2011.

- Meehl, G. A., W. M. Washington, B. D. Santer, W. D. Collins, J. M. Arblaster, A. Hu, D. M. Lawrence, H. Teng, L. E. Buja, and W. G. Strand (2006), Climate change projections for the twenty-first century and climate change commitment in the CCSM3, *J. Clim.*, *19*, 2597–2616, doi:10.1175/JCLI3746.1.
- Min, S.-K., X. Zhang, F. W. Zwiers, and T. Agnew (2008), Human influence on Arctic sea ice detectable from early 1990s onwards, *Geophys. Res. Lett.*, *35*, L21701, doi:10.1029/2008GL035725.
- Mlawer, E. J., S. J. Taubman, P. D. Brown, M. J. Iacono, and S. A. Clough (1997), Radiative transfer for inhomogeneous atmospheres: RRTM, a validated correlated-k model for the longwave, *J. Geophys. Res.*, *102*, 16,663–16,682, doi:10.1029/97JD00237.
- Morrison, H., G. de Boer, G. Feingold, J. Harrington, M. D. Shupe, and K. Sulia (2012), Resilience of persistent Arctic mixed-phase clouds, *Nat. Geosci.*, *5*, 11–17, doi:10.1038/NGEO1332.
- Parkinson, C. L., and J. C. Comiso (2013), On the 2012 record low Arctic sea ice cover: Combined impact of preconditioning and an August storm, *Geophys. Res. Lett.*, *40*, 1356–1361, doi:10.1002/grl.50349.
- Perovich, D. K., T. C. Grenfell, B. Light, and P. V. Hobbs (2002), Seasonal evolution of the albedo of multiyear Arctic sea ice, *J. Geophys. Res.*, *107*(C10), 8044, doi:10.1029/2000JC000438.
- Perovich, D. K., T. C. Grenfell, J. A. Richter-Menge, B. Light, W. B. Tucker III, and H. Eicken (2003), Thin and thinner: Sea ice mass balance measurements during SHEBA, *J. Geophys. Res.*, *108*(C3), 8050, doi:10.1029/2001JC001079.
- Perovich, D. K., B. Light, H. Eicken, K. F. Jones, K. Runciman, and S. V. Nghiem (2007), Increasing solar heating of the Arctic Ocean and adjacent seas, 1979–2005: Attribution and role in the ice-albedo feedback, *Geophys. Res. Lett.*, *34*, L19505, doi:10.1029/2007GL031480.
- Persson, P. O. G. (2012), Onset and end of the summer melt season over sea ice: Thermal structure and surface energy perspective from SHEBA, *Clim. Dyn.*, *39*, 1349–1371, doi:10.1007/s00382-011-1196-9.
- Persson, P. O. G., C. W. Fairall, E. L. Andreas, P. S. Guest, and D. K. Perovich (2002), Measurements near the atmospheric surface flux group tower at SHEBA: Near-surface conditions and surface energy budget, *J. Geophys. Res.*, *107*(C10), 8045, doi:10.1029/2000JC000705.
- Pithan, F., B. Medeiros, and T. Mauritsen (2014), Mixed-phase clouds cause climate model biases in Arctic wintertime temperature inversions, *Clim. Dyn.*, *43*, 289–303, doi:10.1007/s00382-013-1964-9.
- Polyakov, I., et al. (2007), Observational program tracks Arctic Ocean transition to a warmer state, *Eos Trans. AGU*, *88*, 398–399, doi:10.1029/2007EO400002.
- Schröder, D., D. L. Feltham, D. Flocco, and M. Tsamados (2014), Arctic sea-ice minimum predicted by spring melt-pond fraction, *Nat. Clim. Change*, *4*, 353–357, doi:10.1038/nclimate2203.
- Sedlar, J., and A. Devasthale (2012), Clear-sky thermodynamic and radiative anomalies over a sea ice sensitive region of the Arctic, *J. Geophys. Res.*, *117*, D19111, doi:10.1029/2012JD017754.
- Sedlar, J., M. Tjernström, T. Mauritsen, M. Shupe, I. Brooks, O. Persson, C. Birch, C. Leck, A. Sirevaag, and M. Nicolaus (2011), A transitioning Arctic surface energy budget: the impacts of solar zenith angle, surface albedo and cloud radiative forcing, *Clim. Dyn.*, *37*, 1643–1660, doi:10.1007/s00382-010-0937-5.
- Serreze, M. C., and J. A. Francis (2006), The arctic amplification debate, *Clim. Change*, *76*, 241–264, doi:10.1007/s10584-005-9017-y.
- Serreze, M. C., and R. G. Barry (2011), Processes and impacts of Arctic amplification: A research synthesis, *Global Planet. Change*, *77*, 85–96, doi:10.1016/j.gloplacha.2011.03.004.
- Serreze, M. C., M. M. Holland, and J. Stroeve (2007), Perspectives on the Arctic's shrinking sea-ice cover, *Science*, *315*, 1533–1536, doi:10.1126/science.1139426.
- Shimada, K. (2006), Pacific Ocean inflow: Influence on catastrophic reduction of sea ice cover in the Arctic Ocean, *Geophys. Res. Lett.*, *33*, L08605, doi:10.1029/2005GL025624.
- Shupe, M. D., P. O. G. Persson, I. M. Brooks, M. Tjernström, J. Sedlar, T. Mauritsen, S. Sjogren, and C. Leck (2013), Cloud and boundary layer interactions over the Arctic sea ice in late summer, *Atmos. Chem. Phys.*, *13*, 9379–9400, doi:10.5194/acp-13-9379-2013.
- Simmonds, I., and I. Rudeva (2012), The great Arctic cyclone of August 2012, *Geophys. Res. Lett.*, *39*, L23709, doi:10.1029/2012GL054259.
- Spreen, G., L. Kaleschke, and G. Heygster (2008), Sea ice remote sensing using AMSR-E 89 GHz channels, *J. Geophys. Res.*, *113*, C02S03, doi:10.1029/2005JC003384.
- Snow, Water, Ice and Permafrost in the Arctic (2011), *Executive Summary: Snow, Water, Ice and Permafrost in the Arctic, Arctic Monitoring and Assessment Programme (AMAP)*, 15 pp., SWIPA, Oslo, Norway.
- Tjernström, M. (2005), The summer Arctic boundary layer during the Arctic Ocean Experiment 2001 (AOE-2001), *Bound.-Layer Meteorol.*, *117*, 5–36.
- Tjernström, M., C. Leck, P. O. G. Persson, M. L. Jensen, S. P. Oncley, and A. Targino (2004), The summertime Arctic atmosphere: Meteorological measurements during the Arctic Ocean Experiment (AOE-2001), *Bull. Am. Meteorol. Soc.*, *85*, 1305–1321, doi:10.1175/BAMS-85-9-1305.
- Tjernström, M., et al. (2012), Meteorological conditions in the central Arctic summer during the Arctic Summer Cloud Ocean Study (ASCOS), *Atmos. Chem. Phys.*, *12*, 1–27, doi:10.5194/acp-12-1-2012.
- Tjernström, M., et al. (2014), The Arctic Summer Cloud Ocean Study (ASCOS): Overview and experimental design, *Atmos. Chem. Phys.*, *14*, 2823–2869, doi:10.5194/acp-14-2823-2014.
- Uttal, T., et al. (2002), The surface heat budget of the Arctic, *Bull. Am. Meteorol. Soc.*, *83*, 255–275.
- Woods, C., R. Caballero, and G. Svensson (2013), Large-scale circulation associated with moisture intrusions into the Arctic during winter, *Geophys. Res. Lett.*, *40*, 4717–4721, doi:10.1002/grl.50912.
- Zhang, J., R. Lindsay, A. Schweiger, and I. Rigor (2012), Recent changes in the dynamic properties of declining Arctic sea ice: A model study, *Geophys. Res. Lett.*, *39*, L20503, doi:10.1029/2012GL053545.